Catalysis Today xxx (xxxx) xxx–xxx

Contents lists available at ScienceDirect

Catalysis Today

journal homepage: www.elsevier.com/locate/cattod

Towards rigorous multiscale flow models of nanoparticle reactivity in chemical looping applications

Stefan Andersson[a,*], Stefan Radl[b], Ingeborg-Helene Svenum[a], Stephen A. Shevlin[c], Z. Xiao Guo[c], Shahriar Amini[a]

[a] SINTEF, P.O. Box 4760 Torgarden, 7465 Trondheim, Norway
[b] Graz University of Technology, Institute of Process and Particle Engineering, Inffeldgasse 13/III, 8010 Graz, Austria
[c] Department of Chemistry, University College London, Gower Street, London WC1E 6BT, United Kingdom

ARTICLE INFO

Keywords:
Chemical looping
Nanoparticles
Iron oxide
Multiscale modeling
Kinetic Monte Carlo
Flow modeling

ABSTRACT

A multiscale modeling framework is described and applied to the reactivity of iron oxide nanoparticles in a chemical looping reforming (CLR) reactor. At the atomic scale/nanoscale, we have performed kinetic Monte Carlo modeling, guided by Density Functional Theory calculations, on the detailed kinetics of the CH_4 conversion to products as a function of temperature. These results have been post-processed for use in macroscopic models with the goal to integrate process information with materials information. Two levels of macroscopic models have been used to evaluate the performance of the nanoparticles in their final application: (1) a pore-unresolved intra-particle transport model that accounts for limitations via an effective diffusivity and an effectiveness factor, and (2) a fluid-particle multiphase flow model that allows the study of the consequences of clustering and intra-particle transport on overall reactor performance. This modeling approach ultimately leads to better descriptors of material performance that can be used in future materials screening activities.

1. Introduction

Chemical looping [1] is an emerging technology for producing electricity, fuels or chemicals with low CO_2 emissions. In Chemical Looping Combustion (CLC), dual fluidized beds are often used to circulate the solid oxygen carrier particles, which provide the oxygen for combustion in the fuel reactor. The reduction of the particles in the fuel reactor makes it necessary to circulate oxygen carriers to the other fluidized bed, the air reactor, where the particles are oxidized. Subsequently, they are circulated back to the fuel reactor for another combustion cycle, and so on. The separation of fuel from air has several positive features: the combustion process becomes simpler, the combustion efficiency is – in principle – higher than for standard power plants, NO_x emissions are limited since nitrogen is not present in the fuel reactor, and CLC generates an almost pure CO_2 stream, after condensation of water vapor [1]. However, to achieve the necessary efficiency gains of CLC in practice, efficient oxygen carriers with high oxygen capacity, high reactivity, and low attrition rate are crucial.

Chemical Looping Reforming (CLR) [1,2] techniques follow the same basic outline as CLC but focus on the catalytic production of CO and H_2, for use in chemical industry, or, in the latter case, as a clean fuel. In Fig. 1 a schematic overview of the CLR process is presented including typical physical conditions. Typical oxygen carrier materials (MeO) are for instance NiO, CuO, Mn_2O_3, and Fe_2O_3. The CLR process uses less air than CLC, such that only partial oxidation of the oxygen carrier particles is achieved. In CLR, CH_4 reacts with a metal oxide in order to extract individual hydrogen atoms. The H atoms react together forming H_2 that subsequently desorbs from the surface. In the process the metal oxide is reduced by the extraction of oxygen by reaction with carbon from methane, forming CO. One of the aims of our study is to evaluate the suitability of the different iron oxides for CLR. A reduction sequence $Fe_2O_3 \rightarrow Fe_3O_4 \rightarrow FeO \rightarrow Fe$ is then expected. The present work concentrates on magnetite, Fe_3O_4, which forms naturally when hematite, Fe_2O_3, is reduced. At elevated temperatures Chemical Looping Combustion might occur instead, where hydrogen and carbon are completely oxidized to form H_2O and CO_2.

Kinetic studies of unsupported iron nanoparticles have revealed improved reactivity, reduced mass resistance and enhanced heat transfer [3]. However, at temperatures above 450 °C, particle sintering results in coarsening of the particles (up to μm scale), and the observed benefits disappear. In order to utilize the nanostructured materials, it is therefore necessary to endow them with much greater thermal stability. This can be achieved by dispersing the active nano-catalyst within an inert support material, which suppresses coarsening and sintering via

* Corresponding author.
E-mail address: stefan.andersson@sintef.no (S. Andersson).

https://doi.org/10.1016/j.cattod.2019.06.024
Received 1 November 2018; Received in revised form 24 May 2019; Accepted 8 June 2019

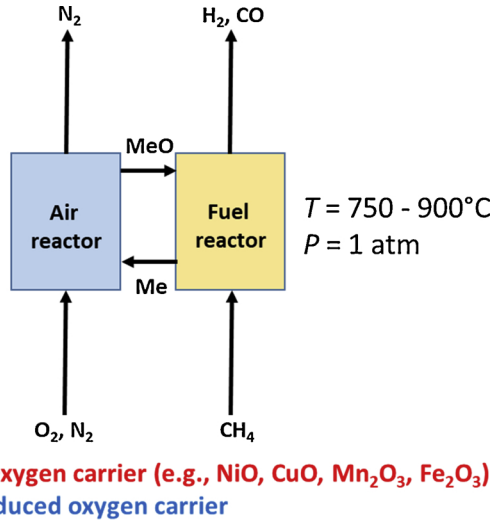

Fig. 1. Schematic representation of complete CLR process, involving reduction of the metal oxide (MeO) under methane to a less oxygen-rich phase (Me). Syngas is outputted from this reactor. Meanwhile, the reduced material is re-oxidized in a separate air reactor before being fed back into the fuel reactor. Typical physical conditions and common oxygen carrier materials are shown.

physical separation [4,5]. In effect, a "mechanical caging" mechanism stabilizes the nanoparticles in the mesopores of the support material [6]. Such stabilized nano-composites have been successfully synthesised through reverse emulsion processes [7,8], but these routes are neither cost efficient, environmentally friendly, nor viable for large-scale production. More cost effective and "green" synthesis routes are therefore sought.

The available literature on nanostructured oxygen carrier materials mostly considers first-row transition metals, which are then dispersed onto a thermally stabilizing amorphous barium hexaaluminate (BHA) support [4,5,7,9,10]. BHA as the support material has a high sintering temperature and low reactivity towards metal oxides under employed operating conditions. However, substitution of BHA due to cost and in some cases toxicity of Ba-precursors, is desirable.

Modeling studies can be a highly valuable complement to experimental studies. Three different studies have recently been published using Density Functional Theory (DFT) to characterize mechanisms and reaction barriers of CH_4 reacting with a Fe_2O_3 surface [11–13]. Although the calculation setups are quite similar, the studies disagree both regarding detailed mechanisms, as well as the energetics of the individual reactions, indicating fundamental challenges in applying DFT to iron oxides. The mechanism of initial dissociation of CH_4 into CH_3 and H is in all studies found to be occurring on top of a surface Fe atom with the product H atom adsorbed at a surface O site. Still, the calculated reaction barrier height varies between 1 and 2 eV. For our present work, DFT calculations of the related reactions with Fe_3O_4 were performed in order to clarify the important mechanisms, as well as to form a basis for modeling the reaction kinetics.

Focusing on Fe_3O_4 and not the other iron oxides is in part motivated by the experimental observation by Rydén and co-workers [14] that CH_4 reacting with iron oxide initially in the form of Fe_2O_3 gives mainly CLC in the initial phase but shows a period of CO + H_2 formation, i.e., CLR, upon partial reduction of the oxide, most likely to Fe_3O_4. Future endeavours to construct more complete models of CLC and CLR systems should of course include a variety of oxide phases. It is further assumed that the modeled nanoparticles, which are embedded in much larger (μm-sized) carrier particles mainly consisting of an inert support material, have been synthesised such that they are thermally and chemically stable and thereby for instance immune to the effects of sintering. It would also be possible to modify the model to reflect changes in (nano)particle structure if this is expected to occur.

In addition to DFT-based modeling, other simulation approaches (e.g., molecular dynamics and Monte Carlo simulations) are also used to screen materials in the field of carbon capture and beyond. While recent studies made significant progress, e.g., related to high-throughput screening [15,16], they agree on the fact that there are several missing links to practical applications: (i) heat and mass exchange phenomena in the pores of the catalytically active material [17,18] and the reactor are often not considered, (ii) fluid and particle flow is greatly simplified in the reactor model, (iii) slow processes (e.g., sintering and deactivation) are typically not taken into account, and (iv) the ecological footprint associated with implementing a material on a large scale is often not assessed. In summary, it would be necessary to consider the complete life cycle to properly rank materials according to their overall economic and ecological performance. While these missing links are well known already for a number of years [19,20], more efforts are needed to move from "design the material" to a (process) "design with material" [21,22]. A specific shortcoming of most studies is that they are applicable to fixed beds or monoliths only, thus the catalyst is static [23–25].

In the context of our present work, an additional challenge related to designing a process is that the reaction occurs in a dense (i.e., high particle concentration) gas-particle flow: CLR and CLC processes are often performed in so-called fluidized bed (FB) reactors on the large scale, in which the gas-phase reactants are fed with such high speed that the carrier particles are entirely suspended. Consequently, particles are mobile, and behave like a fluid, giving the FB process its name. This type of reactor is used due to its advantageous heat and mass transfer characteristics, as well as the simple particle handling, which allows an extremely efficient exchange of particles between the reactors in a CLC or CLR process. However, due to hydrodynamic instability, particles in FBs are never homogeneously distributed in space: particles cluster and re-disperse dynamically and induce a complex flow pattern [26]. The sizes of these clusters are on the order of 10 to 100 particle diameters, and their formation rate can be characterized by a time scale which is on the order of approximately 10 to 100 ms. These "forgotten" scales (often referred to as "meso-scale structures") also imply deviations from classical FB reactor models that assume a well-mixed gas and particle phase [27,28]. In our present contribution we will demonstrate that these deviations are indeed significant for a CLR process, and hence must be respected when building a multiscale model.

In our present paper we present a multiscale modeling framework for simulating a fluidized bed reactor with specific application to the reactivity of iron oxide nanoparticles in a CLR process. The outline of the paper is as follows. In Section 2 we summarize the methods used. For evaluating the reactivity of the iron oxide nanoparticles at the atomic scale/nanoscale, we have performed kinetic Monte Carlo (kMC) modeling, guided by DFT calculations, on the detailed kinetics of the CH_4 conversion to products as a function of temperature. This has to the best of our knowledge not been previously reported for chemical looping systems. In addition, we have used two levels of "macro models" to evaluate the performance of the nanoparticles in their final application: (i) a pore-unresolved intra-particle transport model that accounts for limitations via an effective diffusivity and an effectiveness factor, as well as (ii) a fluid-particle multiphase flow model that allows us to study the consequences of clustering and intra-particle transport on overall reactor performance. Section 3 presents the results, including (i) details related to the interaction of CH_4 with the iron oxide surface unveiled via DFT, (ii) gas-surface kinetics of decomposition of CH_4 and further reactions of produced H_2 and CO simulated by kMC models, (iii) post-processing of the resulting reaction rates to produce effective rate constants used in our intra-particle transport model, (iv) a reaction analysis and evaluation of intra-particle effectiveness factors, as well as (v) a quantification of meso-scale effects predicted by our multiphase flow model. We close our study with conclusions and an outlook in Section 4.

2. Methods

2.1. Atomic-scale modeling

A Density Functional Theory (DFT) approach was taken to model chemistry on metal oxide surfaces. The VASP code was used in all calculations [29–32], with a plane wave cutoff of 520 eV. The projector augmented wave (PAW) method was used to treat the core electrons [33,34]. All atoms were fully relaxed until the change in force upon ionic displacement was less than 0.01 eV/Å, with the change in energies no greater than 10^{-5} eV. K-point meshes were chosen so that the difference in energies is less than 1 meV. The PBE + U functional is used in all calculations, with the U placed on the d-state of the Fe ions [35]. Literature studies of Fe-oxide materials use several different values for U, including 4.0 eV [36–38], 4.2 eV [39], and 5.0 eV [40]. We use a value of U = 4.2 eV as this gives a good match with experimental values. The Climbing Image Nudged Elastic Band (CI-NEB) method was used in order to determine the activation barriers for chemical reaction [41]. Four images were used in NEB calculations unless otherwise stated. As Fe_3O_4 is ferromagnetic, spin-polarization was used in all calculations. The (111) surface of Fe_3O_4 was chosen, as it is predicted to be the most stable surface [42]. There are six possible surface termination. The termination with tetrahedrally coordinated Fe atoms, and with a second layer of oxygen atoms has been applied here, as it has been found to be the energetically favoured surface under oxygen-rich and oxygen-poor conditions [43].

The kinetic Monte Carlo method [44,45] was used to study the kinetics of the overall reactions occurring at the surface. For all calculations the kmos code was used [46]. The use of kMC allows for the kinetics of a system to be studied with greater accuracy than traditional microkinetic rate equation models. In particular, it allows for resolving a complex reactive system in molecular detail including individual sites and atoms and molecules. At the same time, there is no need to describe the system in atomistic detail, including molecular structures and interactions, such as for molecular dynamics or electronic structure calculations, allowing for fast simulations. In a lattice kMC model one only needs to specify a number of connected sites, populations of atoms and molecules at these sites, and the rates of reaction and transition (diffusion, adsorption, or desorption). Subsequently, a stochastic simulation of the motion and reaction of the species can be carried out, where one process at a time occurs. More information regarding the basics and applications of kMC to surface chemistry in general and catalysis in particular can be found in, e.g., Refs. [44–48].

2.2. Macro-model level 1: Intra-particle transport model

Intra-particle transport accounts for the competition of diffusion with species consumption due to a chemical reaction. Specifically, for the present Computational Fluid Dynamics (CFD) analysis, the following reactions are considered:

$$CH_4 + Fe_3O_4 \rightarrow 2H_2 + CO + Fe_3O_3 \quad (1)$$

$$CO + Fe_3O_4 \rightleftharpoons CO_2 + Fe_3O_3 \quad (2)$$

$$H_2 + Fe_3O_4 \rightleftharpoons H_2O + Fe_3O_3 \quad (3)$$

Reaction (1) is modeled as an irreversible reaction that is first order with respect to both reactants (this is motivated by our discussion in Section 3.1). Reactions (2) and (3) are modeled as reversible reactions, which are first order with respect to reactants and products.

Note that the solid-state product in Reactions (2) and (3) is given as Fe_3O_3, instead of 3FeO. This is done for practical purposes to handle any oxide with a composition in between Fe_3O_4 and FeO, which will be defined as a mixture of Fe_3O_4 and Fe_3O_3. This also takes care of cases that can be described as "oxygen-depleted Fe_3O_4" but have not yet transformed into an FeO-like structure.

An analysis of the kinetics that govern the above reactions (see Section 3.3 for details) indicates that Reaction (1) is comparably slow, that Reaction (2) favors the products and is fast, as well as that Reaction (3) favors the reactants and is comparably slow. Thus, the above reaction network is simplified to

$$CH_4 + 2Fe_3O_4 \rightarrow 2H_2 + CO_2 + 2Fe_3O_3 \quad (4)$$

As discussed in Section 3.3, the conditions that justify the simplified Reaction in (4) are: (i) a temperature between 975 K and 1300 K, as well as (ii) a Fe_3O_4 conversion in the range $0.04 < X_{Fe3O4} < 0.992$. The second condition is met almost everywhere in our simulation (see Section 3.5), and condition (i) is met by considering T = 1200 K.

Reaction progress is expressed using the Fe_3O_4 conversion (square brackets indicate concentrations):

$$X_{Fe_3O_4} = \frac{[Fe_3O_3]}{[Fe_3O_4]_0} \quad (5)$$

Intra-particle transport is analyzed for the simplified reaction network following the work of Yang et al. [49]. Besides Fe_3O_4 conversion, the Thiele modulus defined as

$$\Phi = \frac{d_p}{2}\sqrt{\frac{k'}{D_{eff}}} \quad (6)$$

affects intra-particle concentration profiles, and hence the intra-particle effectiveness factor η. In the above expression D_{eff} is the effective diffusivity of CH_4 in the pores of a carrier particle with diameter d_p, and k' is a modified reaction rate constant:

$$k' = k_1[Fe_3O_4] \quad (7)$$

Here k_1 is the reaction rate constant of Reaction (1) evaluated at the system temperature. Note, as Fe_3O_4 is consumed, k' decreases, and hence also the Thiele modulus decreases. Thus, the intra-particle effectiveness factor η typically increases with Fe_3O_4 conversion (note, an intermediate decrease of η with increasing conversion is possible in case of very high initial Thiele moduli, see Fig. 9 in Section 3.3). Specifically, we evaluate η via [49], considering two temporal stages, i.e., a stage prior and after the formation of a shell in the carrier particle that is depleted of Fe_3O_4. The resulting equations that we evaluate are:

$$\xi_b = \left[\left(\frac{15}{\Phi^2}\right)^{0.6} + (1 - X_{Fe_3O_4})^{0.4}\right]^{1/3}(1 - X_{Fe_3O_4})^{0.2} \quad (8)$$

$$X_0 = \frac{3}{\Phi^2}(\Phi\coth(\Phi) - 1) \quad (9)$$

$$\eta = \begin{cases} X_0, & X_{Fe_3O_4} < X_0 \\ \dfrac{3\xi_b^3}{(\Phi\xi_b)^2}\dfrac{\Phi\xi_b\coth(\Phi\xi_b) - 1}{1 + (1 - \xi_b)[\Phi\xi_b\coth(\Phi\xi_b) - 1]}, & X_{Fe_3O_4} \geq X_0 \end{cases} \quad (10)$$

In the above expression ξ_b is the normalized radius of the shrinking active core (of the carrier particle) in the second temporal stage. X_0 is the Fe_3O_4 conversion at the end of the first temporal stage.

2.3. Macro-model level 2: Fluid-Particle flow model

Since the intra-particle transport model described in the previous sections only accounts for transport within individual particles, an additional model to describe transport exterior to the particles is needed. In our present study we focus on a so-called particle-unresolved Euler-Lagrange (PU-EL) model in which fluid flow exterior of the particles is predicted on a computational grid with a cell size larger than the particle diameter (an illustration of the PU-EL approach is provided in Section 3.4). This expands our previous work on coupled intra-particle (heat) transport and particle flow [50] to reactive fluid-particle flows. The core idea of our coupling strategy is summarized in Fig. 2. Specifically, we rely on three core software tools: (i) ParScale for intra-

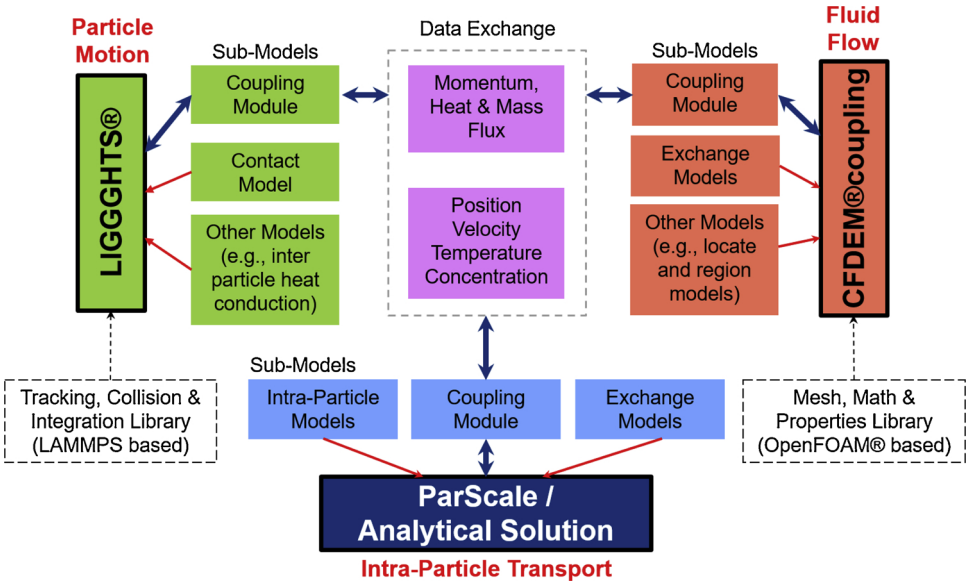

Fig. 2. Model structure used to account for reactive fluid-particle flow that is affected by intra-particle transport.

particle transport (alternatively, we allow the usage of analytical solutions, e.g., for the effectiveness factor as we do in our present work, see Section 2.2), (ii) LIGGGHTS® for particle flow, as well as (iii) CFDEM®coupling for fluid flow and transport exterior of particles (all tools are publicly available via https://github.com/CFDEMproject).

In the context of our present work, coupled PU-EL simulations allow us to predict the spatial distribution of methane, as well as Fe_3O_4 conversion and the intra-particle effectiveness factor from the model of Yang et al. [49]. The latter deviates appreciably from unity in cases where comparably larger particles are considered (e.g., see the results for 1 mm particles summarized in Section 3.5). However, intra-particle effectiveness factors are above 0.99 for the FB application presented in our present work.

In order to quantify the degree of mixing in the system, the transient of the overall (domain-average) Fe_3O_4 conversion is compared with a prediction based on a perfectly mixed gas and particle phase in the system. The latter yields the following differential equations (overbars indicate domain-average quantities, V indicates volume, and $\dot{N}_{CH_4,feed}$ is the molar methane feed rate):

$$V_{tot}\,\partial_t\overline{[CH_4]} = -k_1\overline{[CH_4]}\overline{[Fe_3O_4]}\,\eta\,\eta_{meso}V_{p,tot} + \dot{N}_{CH_4,feed} \quad (11)$$

$$\partial_t\overline{[Fe_3O_4]} = -2k_1\overline{[CH_4]}\overline{[Fe_3O_4]}\,\eta\,\eta_{meso} \quad (12)$$

The meso-scale effectiveness factor η_{meso} expresses how much the reaction is slowed down by incomplete mixing in the gas and solid phase. This factor is extracted from the CFD simulations by a fitting procedure.

3. Results and discussion

3.1. Density functional theory and kinetic Monte Carlo

In order to ascertain the reactivity of Fe_3O_4 in CLR processes, the interaction of relevant species was investigated using DFT. The adsorption geometries of CH_x species on the iron oxide surface are illustrated in Fig. 3. A potential energy diagram of the decomposition of CH_4 to CH_2+H is illustrated in Fig. 4a. We did not include further decomposition steps or explicit subsequent reactions of CO and CO_2 formation in our calculations. It was noted in the Introduction that seemingly similar DFT calculations on CH_4 reactions at Fe_2O_3 gave quite different results [11–13]. This is probably due to calculations converging to different close-lying electronic states by only slight variations of input parameters (such as the U parameter). Similar problems with convergence were encountered in the present calculations on Fe_3O_4, showing for instance a large variation in spin polarization. Since the main purpose of the study was not to provide accurate energetics of all processes involved but to demonstrate a multiscale modeling framework, it was decided to work with a simplified reaction scheme (see below). As for the results of the DFT calculations, CH_4 interacts preferably with the surface tetrahedral Fe atoms (Fe_{tet} site) of Fe_3O_4, where the lowest energy configuration for CH_4 binding is that wherein only two hydrogen atoms are lower than the carbon atom, i.e., an edge-on configuration. The lowest energy structure for CH_3 + H adsorption involves direct adsorption of CH_3 on the O_2 surface oxygen anion. The hydrogen atom prefers to bind in a tilted position to the surface oxygen site that is closest to the Fe_{tet} site (an O_1 site), as illustrated in Fig. 3b. The activation barrier for the first C–H bond activation is 112 kJ/mol. The CH_3 moiety also has a marked preference to bind on the O_2 surface site. Upon activation of the second C–H bond, the H atom forms an O–H bond to the adjacent O_1 site while the CH_2 moiety remains bonded to the O_2 site. The activation barrier for the second C–H bond activation is 202 kJ/mol, and the formation of the CH_2 + H structure is endothermic by 103 kJ/mol relative adsorbed CH_3. The activation of the first C–H bond of CH_4 on Fe_3O_4(111) has a lower barrier than the decomposition of CH_4 on Fe_2O_3(0001) where an activation barrier of 170 kJ/mol has been calculated by DFT [11]. Similar to what was obtained in the present study for the case of Fe_3O_4(111), the activation of the second C–H bond on Fe_2O_3(0001) exhibits a higher barrier compared to the first C–H bond scission. The calculations of Huang et al. [11] predicted that the activation of CH_3 has a barrier of 203 kJ/mol. A similar trend was found in the DFT calculations by Tang and Liu [12] considering free energies at 573.15 K. The previous DFT studies of decomposition of CH_4 on Fe_2O_3(0001) indicate that either dissociation of CH_4 [12,13] or CH_3 [11] is the rate-limiting step. Lacking further information on the analogous reaction at Fe_3O_4(111) it seems reasonable to assume that the rate-limiting step is found among the initial steps of CH_4 decomposition (see below).

Regarding hydrogen formation and adsorption, the exposed Fe_{tet} site dominates the H_2 binding. Atomic hydrogen adsorption is thermodynamically preferred to molecular hydrogen adsorption, as illustrated in Fig. 4b. Two O–H bonds form to adsorb the two hydrogens in neighboring O_1 sites, the hydrogen bonds being oriented away from each other in order to minimize electrostatic energies. Direct recombination of the hydrogen atoms to form H_2 does not happen, this

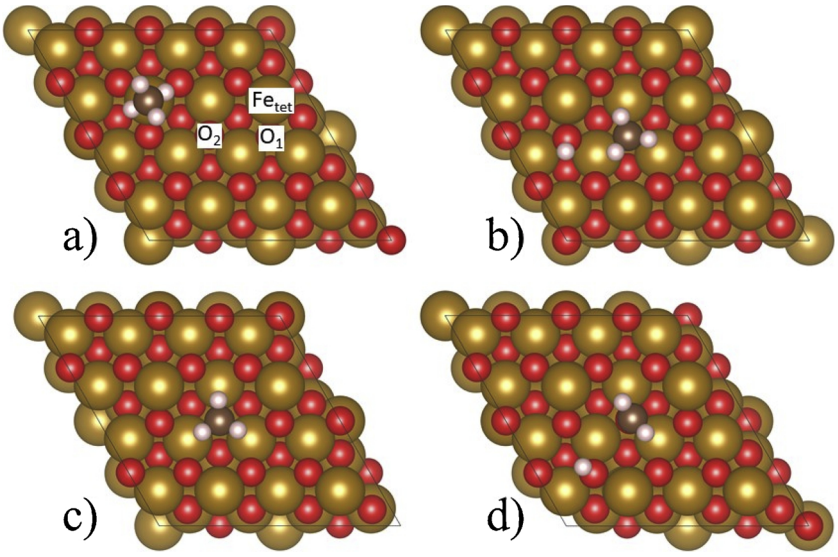

Fig. 3. Thermodynamically stable structures for CH_4 adsorption and molecular fragments produced upon reforming on the $Fe_3O_4(111)$ surface. (a) is CH_4, (b) is CH_3+H, (c) is CH_3, (d) is CH_2+H. Iron is represented by large brown spheres, oxygen by small red spheres, carbon by small dark brown spheres, and hydrogen by small white spheres. Three different sites are indicated in (a): tetrahedrally coordinated Fe atoms (Fe_{tet}), and two different types of surface oxygen atom, one is bound to a tetrahedral Fe and two octahedral Fe atoms (O_1) and the other is bound to three octahedral Fe atoms (O_2). There are four Fe_{tet} sites within the simulation cell. (For interpretation of the references to colour in this figure legend, the reader is referred to the web version of this article.)

would result in a diffusion of 3.75 Å. Rather, H_2 formation proceeds via the Fe_{tet} site. A single hydrogen atom diffuses from the adjacent O_1 site to the Fe_{tet} site. This is an endothermic process with respect to two H atoms situated at two different O_1 sites, being 137 kJ/mol higher in energy. The formation of an H_2O moiety on a surface oxygen site involves the coordination of two hydrogen atoms on an O_2 site of the surface, where two O—H bonds are formed. The H—O—H bond angle, at 108.2°, is similar to that of gas-phase water. This surface oxygen atom that holds the two H atoms is removed from the surface upon release of H_2O. The formation of H_2O with respect to the lowest energy atomic hydrogen structure is endothermic, at 145 kJ/mol, and is associated with an activation barrier of 164 kJ/mol. The formed H_2O is thermodynamically more stable than adsorbed H_2 and unreacted surface oxygen by 15 kJ/mol.

Next, we present a simplified kMC simulation in order to evaluate the overall kinetics of CH_4 reacting with Fe_3O_4. The kMC simulations were started from a clean surface with CH_4 in the gas phase. The CH_4 pressure was 1 bar while sampling different temperatures, ranging from 973 K to 1373 K, in steps of 100 K. It is assumed that all the reactions take place at the surface, and that the concentration of surface O atoms remains constant, meaning that replenishing O from the bulk when a surface O atom has reacted to form CO, CO_2, or H_2O is effectively instantaneous compared to the time scale of the reactions. The assumption that consumed lattice oxide in the surface is replaced by O from lower layers is valid if the rate of O diffusion from bulk to surface is relatively fast, and if the reactions occur in the initial stages of Fe_3O_4 reduction, such that there is a significant reserve of O atoms. The reactions included in the kMC simulation are listed in Table 1. In addition, diffusion processes of CH_3 and H were also accounted for. The decomposition of CH to CH_2 was included in the model, in addition to the formation of H_2O and H_2 upon decomposition of CH_4 and CH_3.

Table 1
Reactions considered in the kMC simulations, where (g) refers to species in the gas phase. $O_{lattice}$ refers to an O atom in the $Fe_3O_4(111)$ surface.

Reactions		
CH_4 (g) ⇌ CH_4	CO ⇌ CO (g)	H + H ⇌ H_2
CH_4 ⇌ CH_3 + H	CO + $O_{lattice}$ ⇌ CO_2	H_2 ⇌ H_2(g)
CH_4 (g) ⇌ CH_3 + H	CO_2 ⇌ CO_2 (g)	H + H + $O_{lattice}$ ⇌ H_2O
CH_3 ⇌ CH_2 + H		H_2O⇌ H_2O (g)

Further decomposition of CH_2 was not considered explicitly, and the rate of formation of CH_2 was assumed to be equal to the combined rates of CO and CO_2 formation with the reverse reaction to produce CH_4 being insignificant due to rapid loss of hydrogen from the surface in subsequent reactions. This is a simplification of the overall decomposition process, but it was partly motivated by challenges in achieving converged DFT results, potentially due to difficulties either in applying the U correction, spin polarization, or the combination of the two (see above). The interactions of H_2, H_2O, CO and CO_2 with the iron oxide surfaces were also modeled separately at a pressure of 1 bar, respectively, to further address the formation of H_2/H_2O and CO/CO_2. The input parameters for the kMC simulations are mainly based on the obtained DFT values described above. The results of running the kMC models have been summarized as turnover frequencies (TOFs), i.e., rates per surface site, for given overall Reactions (1)–(5) discussed in Section 2.2. The TOFs are used in the calculation of rate constants in the next section and are presented in Table 2.

3.2. Calculation of rate constants

The turnover frequencies as calculated in the kMC calculations

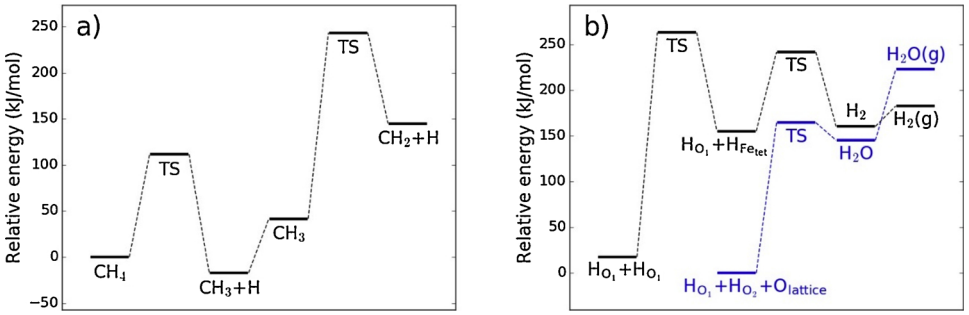

Fig. 4. Relative energy vs. reaction coordinate for a) CH_4 decomposition and b) H_2 and H_2O formation. The energies of CH_3 to CH_2+H include the energy of 0.5 H_2(g) such that the overall composition is CH_4 and energies are relative to adsorbed CH_4. The labels O_1, O_2 and Fe_{tet} refers to H at different adsorption sites (see Fig. 3), and $O_{lattice}$ refers to an O atom in the $Fe_3O_4(111)$ surface.

Table 2
Turnover frequencies (TOFs) for the reactions with Fe_3O_4 surfaces at different temperatures as obtained from kMC simulations. For details see the text.

Reactants	Products	TOF/s^{-1} 973 K	1073 K	1173 K	1273 K	1373 K
CH_4 + Fe_3O_4	CH_2 + Fe_3O_4	0.875	10.1	48.0	76.5	62.8
H_2 + Fe_3O_4	H_2O + Fe_3O_3	0.0657	0.990	8.06	45.0	220
CO + Fe_3O_4	CO_2 + Fe_3O_3	1.10×10^4	7.06×10^3	4.77×10^3	3.35×10^3	2.44×10^3
CO_2 + Fe_3O_3	CO + Fe_3O_4	293	157	104	66.0	37.1
H_2O + Fe_3O_3	H_2 + Fe_3O_4	0.0258	94.5	669	5.91×10^3	2.91×10^4

cannot be directly used in kinetic models that do not explicitly consider surface reactions, but only volumetric rate constants based on the (homogeneous) concentration of reactive particles. It is therefore necessary to post-process the rate data to reflect the size and shape of the particles, as well as the particle surface area that is available for reaction. This procedure will be system-specific and depends on a number of assumptions. We have chosen a purely geometric approach based on the following assumptions:

(1) Reaction only occurs on the surface of a geometric shape representing the reactive particle, i.e., the particle is non-porous, and reactants do not diffuse into the bulk of the particle.
(2) The reactivity of the particle surface does not change from the ideal (flat) surface that has been modeled in the kMC simulations.
(3) Oxygen diffusion from the bulk to the particle surface is significantly faster than any gas-surface reaction.
(4) The shape of the particle does not change as an effect of reaction.
(5) The reactive particles are independent and do not affect each other.

This should be seen as a "zeroth order" model, since these assumptions describe an idealized case where the reactivity only depends on the initial shape and size of the reactive particle. However, the model can be modified to reflect more physically realistic conditions. For instance, the surfaces of small nanoparticles are not likely to be smooth but to have a relatively high density of steps, with presumably higher reactivity than the flat surface, due to the large curvature of the surface. This could have a profound effect on the reactivity of the particle also considering the "normal" non-ideality of any real surface. To correct the simple model outlined above one then needs an estimate of the surface step density, and to also use data from DFT and kMC calculations of reactions at steps.

In Fig. 5 some examples of typical reactive particle geometries are illustrated. These include (1) a square block embedded in a support with only one face of the block available for reaction, (2) a free spherical particle, and (3) a spherical particle embedded on a support (with only half the surface available for reaction. Cases (2) and (3) are the ones considered in this work, since they will represent a micrometer-sized reactive particle and a nanometer-sized embedded reactive particle, respectively.

The rate constants are calculated from the TOFs from the kMC simulations as follows. First, a surface rate (i.e., a rate per unit area) of the reactive particle is calculated as:

$$r_{surf} = \rho_{sites} \nu_{TOF} \tag{13}$$

where ρ_{sites} is the site density and ν_{TOF} is the TOF for a given reaction. The rate of the reacting solid (per unit volume) is defined as

$$r_{solid} = r_{surf} \frac{A_{avail}}{V_{part}} \tag{14}$$

Here A_{avail} is the surface area that is available for reaction and V_{part} is the volume of the reactive particle (Fig. 5). Volumetric gas-particle (2nd order) rate constants have subsequently been calculated as

$$k_{gas-part} = \frac{r_{solid}}{c_{gas} c_{part}} \tag{15}$$

where c_{gas} and c_{part} are the volumetric molar concentrations of gas phase reactant and reactive particle, respectively. The gas concentration is calculated as

$$c_{gas} = \frac{n_{gas}}{V_{gas}} = \frac{p_{gas}}{RT} \tag{16}$$

where n_{gas} is the amount of gas-phase reactant and V_{gas} the corresponding volume at a given pressure and temperature. The last equality follows from the ideal gas law and p_{gas} is the (partial) pressure of the gas phase reactant as specified in the kMC simulations. The concentration of the reactive particle also refers to the kMC simulations, which only considers the surface of the reactive particle and no other parts of the systems, was calculated as

$$c_{part} = \frac{n_{solid}}{V_{solid}} = \frac{\rho_{solid}}{M_{solid}} \tag{17}$$

Here, n_{solid}, V_{solid}, ρ_{solid}, and M_{solid} refer to the amount, volume, density and molar mass of the reactive particle, respectively. The rate constant can therefore be written as

$$k_{gas-part} = \frac{RTM_{solid}}{p_{gas}\rho_{solid}} r_{solid} = \frac{RTM_{solid}\rho_{sites}A_{avail}}{p_{gas}\rho_{solid}V_{part}} \nu_{TOF} \tag{18}$$

These rate constants have been calculated for the temperatures at which the kMC simulations were performed and fitted to an Arrhenius expression

$$k_{gas-part}(T) = AT^{\beta}\exp(-E_a/RT) \tag{19}$$

The parameters are given in Table 3 for the two cases of 1 µm spherical particles and 10 nm embedded spherical particles, corresponding to case 2 and case 3 in Fig. 5, respectively. In this analysis it is additionally assumed that the reaction of CH_4 with Fe_3O_4 exclusively leads to production of CO and H_2, since there is experimental evidence to indicate that CH_4 reacting with Fe_3O_4 would selectively lead to CO + H_2 formation [14] (see Introduction). The simple kMC model described in the previous section was only run to simulate the consumption of CH_4 at the surface and not the final product distribution, due to the exceptionally computationally demanding DFT calculations that would have been needed to evaluate all reaction steps. The main motivation

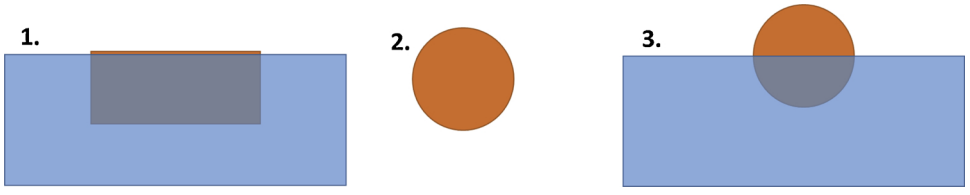

Fig. 5. Three specific cases of (embedded) reactive particles: (1) Square block with only flat surface exposed, (2) Spherical particle with whole surface exposed, and (3) Embedded spherical particles (half surface exposed).

Table 3
Arrhenius parameters for the reactions with Fe_3O_4 reactive particles. For details see the text.

Reactants	Products	A/cm^3 mol^{-1}s^{-1}	β	E_a/kJ/mol
1 μm particle				
CH_4 + Fe_3O_4	CO + 2 H_2 + Fe_3O_3	2.34×10^9	0	132
H_2 + Fe_3O_4	H_2O + Fe_3O_3	5.29×10^{13}	0	234
CO + Fe_3O_4	CO_2 + Fe_3O_3	3.09×10^{16}	−3.38	0
CO_2 + Fe_3O_3	CO + Fe_3O_4	6.20×10^{18}	−4.80	0
H_2O + Fe_3O_3	H_2 + Fe_3O_4	2.14×10^{21}	0	376
10 nm embedded particle				
CH_4 + Fe_3O_4	CO + 2 H_2 + Fe_3O_3	1.17×10^{11}	0	132
H_2 + Fe_3O_4	H_2O + Fe_3O_3	2.65×10^{15}	0	234
CO + Fe_3O_4	CO_2 + Fe_3O_3	1.55×10^{18}	−3.38	0
CO_2 + Fe_3O_3	CO + Fe_3O_4	3.10×10^{20}	−4.80	0
H_2O + Fe_3O_3	H_2 + Fe_3O_4	1.07×10^{23}	0	376

behind this study is to demonstrate the simulation framework and the flow of information between scales. A future refined study of this reaction should of course consider also the possibilities of forming CO_2 and H_2O directly as well. It should also be pointed out that since the calculation of the rate constants is based on pure geometrical differences there is a constant factor 50 difference between the rate constants involving the 1 μm particles and 10 nm embedded particles due to larger available area-to-volume ratio for the smaller particles.

3.3. Reaction analysis and insights from intra-particle transport model

The rate constants of the three considered reactions in the CFD analysis (i.e., irreversible methane conversion, as well as the reversible reactions of CO and H with Fe_3O_4 as in Table 3 and as discussed in Section 2.2) are shown in Fig. 6. While Reactions (1) (i.e., CH_4 consumption) and (3) (i.e., steam formation from H_2) show typical Arrhenius behaviour, the rate of Reaction (2) (i.e., CO conversion to CO_2) decreases with increasing temperature. However, Reaction (2) is at least an order of magnitude faster than the other reactions. Thus, Reactions (1) (CH_4 consumption) and (3) (steam formation from H_2) are rate limiting near 1200 K.

Next, we consider the equilibrium parameter defined as the ratio of the forward rate constant and the reverse rate constant. Specifically, we have considered Reactions (2) (i.e., reversible CO conversion; see first paragraph in Section 2.2) and (3) (i.e., reversible H_2 conversion), as well as the Arrhenius parameters in Table 3 to calculate $k_{gas\text{-}part}/k_{r,gas\text{-}part}$ via Eqn. 19. We note in passing that for 50% Fe_3O_4 conversion, this ratio equals the equilibrium ratio of product and reactant gas concentration. As shown in Fig. 7, the equilibrium for Reaction (2) is on the gas product side, while for Reaction (3) it is on the gas reactant side for temperatures above 975 K.

At 1200 K, and for Fe_3O_4 conversions between 0.1 and 0.9, the product-to-reactant distribution is such that CO_2 and H_2 formation is favoured (Fig. 8). Only for very low conversions (i.e., $X_{Fe3O4} < 0.04$; see Reaction (3) in Fig. 8), H_2O formation is favoured, while only at very high Fe_3O_4 conversions (i.e., $X_{Fe3O4} > 0.992$; see reaction 2 in Fig. 8) CO formation is favoured.

Thus, over a wide range of conversions the second slow reaction (i.e., H_2O formation) is not favoured. In addition, the conversion of CO to CO_2 can be assumed to be fast and complete. In summary, the inspection of rate constants and equilibrium parameters motivates our assumption that CH_4 consumption is the rate limiting step, as well as that our simplified Reaction (4) discussed in Section 2.2 is appropriate. The assumption of CH_4 consumption being the rate limiting step also simplifies the analysis of intra-particle transport, for which results are presented next.

As seen in Fig. 9, intra-particle transport is not limiting for fluidized beds containing 100 μm carrier particles and the 10 nm grains (i.e., the fast reaction; this case is indicated as "base case" in Fig. 9). At 1200 K pore diffusion becomes limiting roughly for 1 mm particles, while for 2.5 mm grains it greatly affects the overall reaction rate. Thus, at the given process temperature and in typical FB applications, only grains with a size significantly smaller than 10 nm would be necessary to cause intra-particle transport to become limiting.

3.4. Fluid-particle flow simulation setup

To demonstrate the developed multiscale modeling approach, we next consider a small-scale fluidized bed CLR reactor. Specifically, as the base case we consider 10 nm Fe_3O_4 grains that are hosted by $d_p = 100$ μm carrier particles with a porosity of $\varepsilon_p = 0.5$, a tortuosity of $\tau = 1$, a particle density of 4000 kg/m^3, as well as an initial Fe_3O_4 mass fraction of $w_{Fe3O4} = 0.15$. The system pressure is 2.0 MPa, the reaction is considered to occur under isothermal conditions at T = 1200 K, and a pure methane feed stream is considered at the inlet of the FB. These settings are in line with our previous study [51] that considered only Reaction (1). Thus, the initial reactant concentrations are $[Fe_3O_4]_0 = 2.59$ kmol/m^3 and $[CH_4]_{in} = 0.200$ kmol/m^3. The inlet gas density, kinematic viscosity, heat conductivity, Prandtl number and diffusivity (of methane in the product gas consisting of CO_2 and H_2) are $\rho_{CH4} = 3.21$ kg/m^3, $\nu_{CH4} = 1.44 \times 10^{-5}$ m^2/s, $\lambda_{CH4} = 7.70 \times 10^{-2}$ W/m/K, Pr = 0.704, and $D_{CH4} = 2.05 \times 10^{-5}$ m^2/s, respectively. Considering the porosity and tortuosity of the carrier particles, the effective diffusivity of methane in the pores of the particles is $D_{eff} = 1.03 \times 10^{-5}$ m^2/s (here we assume that pores are wide enough such that classical diffusion describes transport reasonably well; Knudsen effects are not considered in our present work).

The methane feed rate is based on a fixed gas speed at the inlet. For the latter, 2.5 times the minimal fluidization speed is chosen, which

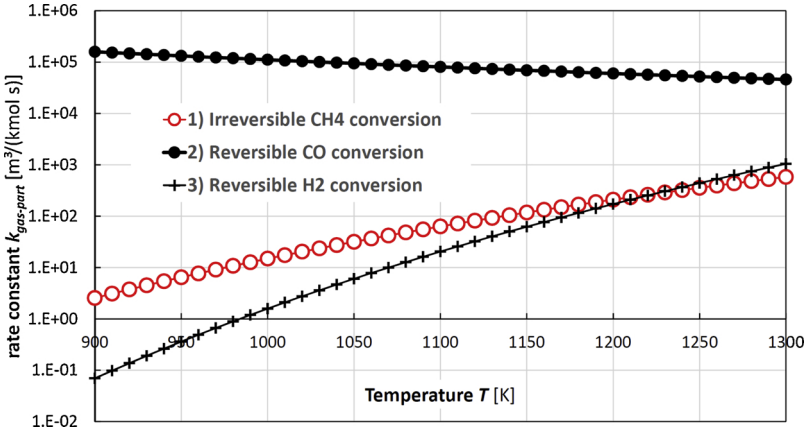

Fig. 6. Forward reaction rate constants for the three most important reactions versus temperature (reactions as discussed in Section 2.2).

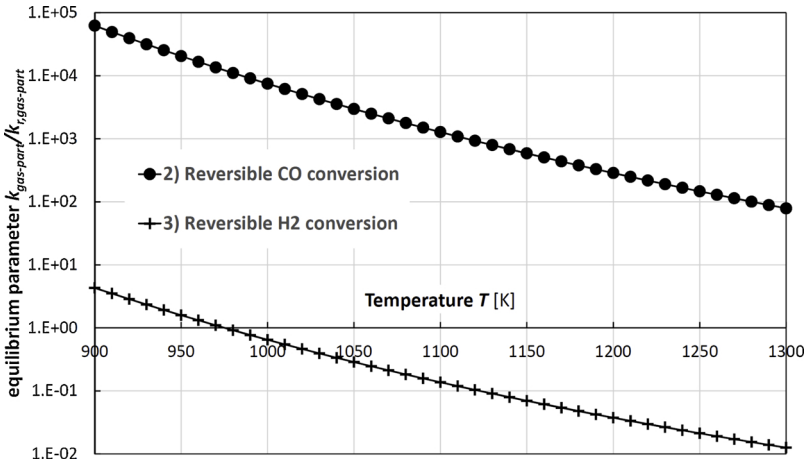

Fig. 7. Equilibrium parameter for reaction (2) (CO conversion to CO_2), as well as reaction (3) (H_2 conversion to H_2O) versus temperature calculated from reaction rate constants (Eq. (19)).

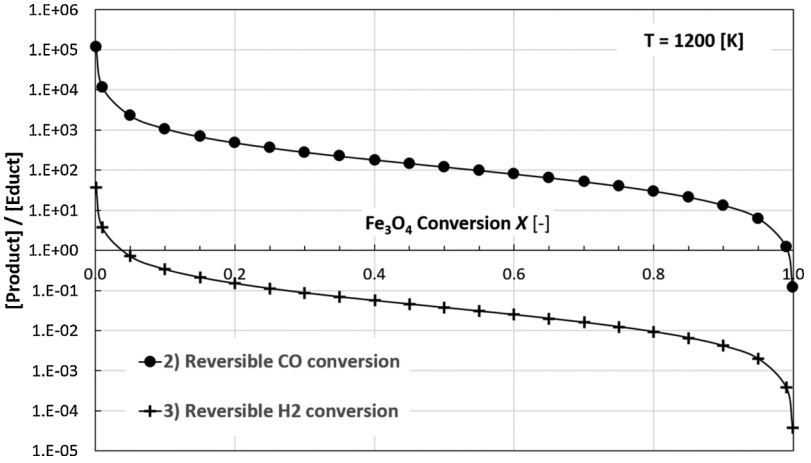

Fig. 8. Ratio of product and reactant (educt) concentration versus Fe_3O_4 conversion for Reaction (2) (i.e., CO conversion to CO_2), as well as Reaction (3) (H_2 conversion to H_2O) at 1200 K.

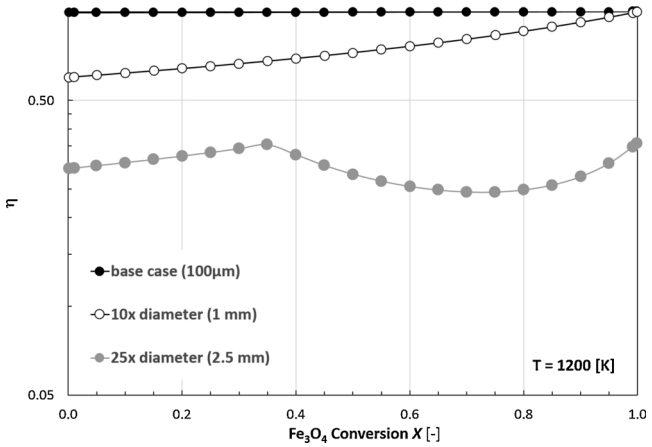

Fig. 9. Effectiveness factor for Reaction (1) (i.e., methane conversion) at 1200 K versus Fe_3O_4 conversion for various carrier particle sizes and 10 nm grains.

yields 0.0352 m/s. The computational domain has a size of $L \times W \times H = 85\ d_p \times 6\ d_p \times 341\ d_p$ and is filled with 50,000 particles (see Fig. 10 for an illustration). The Eulerian grid size resolution is $\Delta_g = 2\ d_p$, and the calculation time step is chosen to ensure a maximum Courant number below 0.2.

3.5. Insights from the fluid-particle flow model

Fig. 11 illustrates the reaction progress, and how it is affected by time and reactivity. Panel a) indicates a rapid reaction which leads to significant solid consumption already after 0.05 s. For such a rapid reaction, Fe_3O_4 is consumed primarily near the CH_4 inlet, leading to strong gradients in the local solids concentration. Due to particle motion induced by the fluidizing gas, these gradients manifest in thin (mainly vertically oriented) streaks of particles with low Fe_3O_4 concentration (see panel a, bottom row). These streaks are still visible for the intermediate reaction rate (see panel b), however, to a much lower extent. For the slowest reaction considered (i.e., the 1 µm grains, see panel c), the Fe_3O_4 concentration distribution is virtually uniform. This can be explained by solids mixing being faster than the chemical reaction.

In Fig. 12 we highlight the CH_4 concentration in the pores of the carrier particles, i.e., the concentration that is relevant for evaluating the reaction rate. Similar as for the solids concentration, in case of a fast reaction (see panel a) there are regions with extremely low CH_4 concentration. Again, this indicates that the chemical reaction is faster than mixing in the system and the supply of methane via the fluidizing gas. Interestingly, the profiles of the CH_4 concentration in the pores is more uniform and does not show the fine streaks observed in Fig. 11. This is due to the fact that mixing of gases in the fluidized bed is more efficient (due to the higher molecular diffusivity, as well as dispersion due to turbulent fluctuations in the gas).

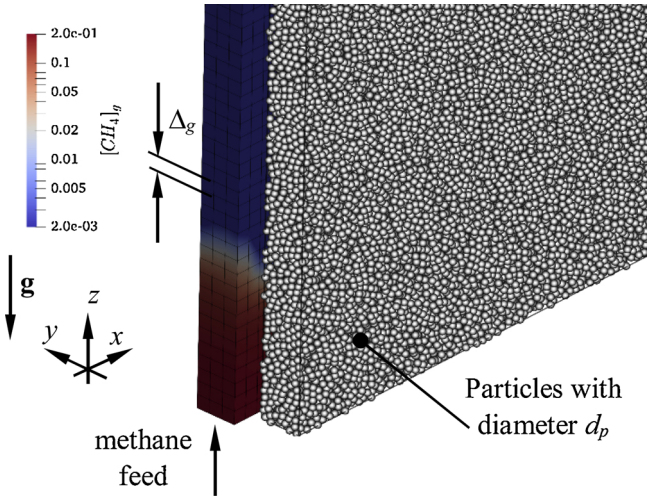

Fig. 10. Illustration of the gas-particle simulation setup (particles are shifted into the –y direction to improve clarity; colors indicate the methane concentration).

Finally, we illustrate CH_4 concentration gradients (but this time in the bulk of the gas phase) in Fig. 13. Clearly, a rapid reaction leads to strong gradients of the gas phase reactant, and a "finger" of high CH_4 concentration is clearly observable after 0.2 s of simulated time (see panel a, bottom row). This finger is caused by (i) the locally slowed down reaction (since the solid reactant is locally depleted), and (ii) the complex solids flow pattern.

3.5.1. Comparison with fixed bed operation (1 mm carrier particles)

To contrast the findings for the fluidized bed discussed above, a simulation considering a fixed bed reactor has been performed. Therefore, only the carrier particle size was increased by a factor of 10, and all other parameters were chosen to be identical to the base case scenario. The results (see Fig. 14) indicate the formation of a clear reaction front in the bed, which manifests itself in (i) the profiles of the reactants (see panels b–d), as well as (ii) the effectiveness factor (see panel e). Most important, the effectiveness factor is non-uniform, and close to unity near the reaction front. The reason for this is that near the front the solid phase reactant is already partially consumed, which slows down the reaction (i.e., the modified reaction rate constant in (7) decreases with decreasing Fe_3O_4 concentration). Note, that in our simulations the effectiveness factor is set to zero in case the solid phase reactant is zero (and hence the reaction completed). A second key finding is that the reaction front seems to penetrate faster into the bed near the lateral walls of the reactor. This can be explained by considering the gas-phase flow field (see panel a): near the wall porosity fluctuations lead to a locally higher gas speed, and hence faster CH_4 transport into the bed. This leads to a higher reaction rate, and hence a faster penetration of the reaction front near the wall.

Finally, we return to our fluidized bed case, and aim on illustrating effects due to incomplete mixing. Specifically, we illustrate in Fig. 15 the average Fe_3O_4 conversion versus time, and compare simulated data with the results of the simple model given by Eqs. (11) and (12). We find that setting the meso-scale effectiveness factor η_{meso} to unity (see dashed lines) leads to a significant overprediction of the conversion. Choosing $\eta_{meso} = 0.58$ leads to a much better agreement of our simple model with the CFD-simulated conversion profile. Interestingly, this meso-scale effectiveness factor appears to fit our data for all three

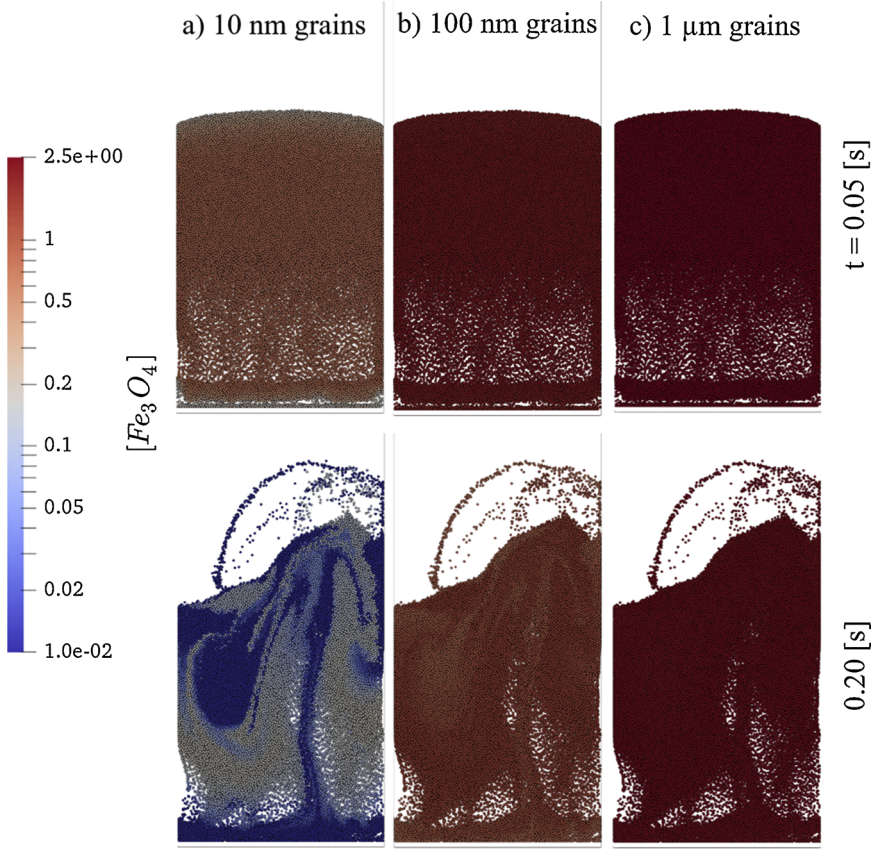

Fig. 11. Distribution of the Fe_3O_4 concentration for different grain sizes and two different times (base case scenario with 100 µm carrier particles).

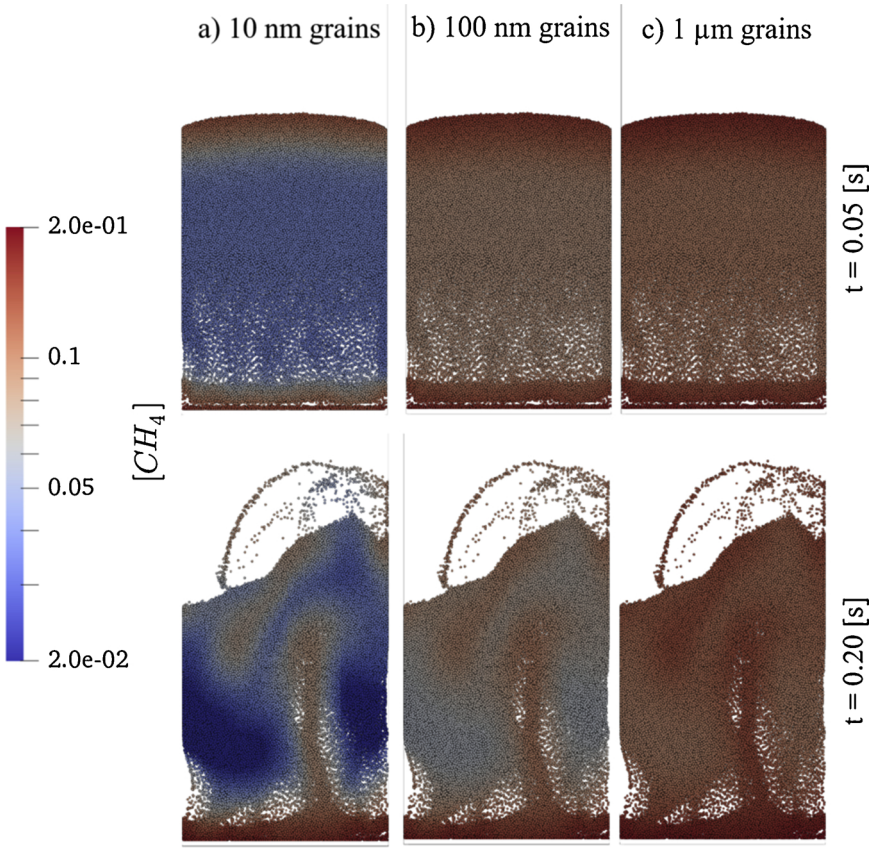

Fig. 12. CH_4 concentration in the pores of the carrier particles for different grain sizes and two different times (base case scenario with 100 µm carrier particles).

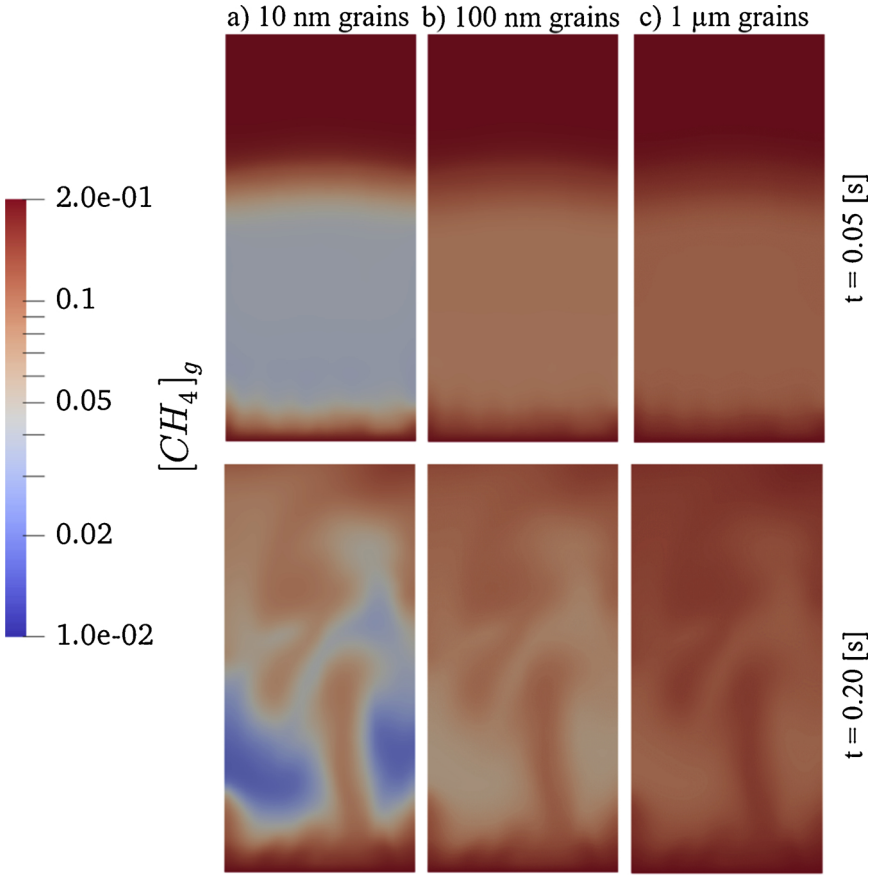

Fig. 13. CH_4 gas phase concentration for different grain sizes and two different times (base case scenario with 100 µm carrier particles).

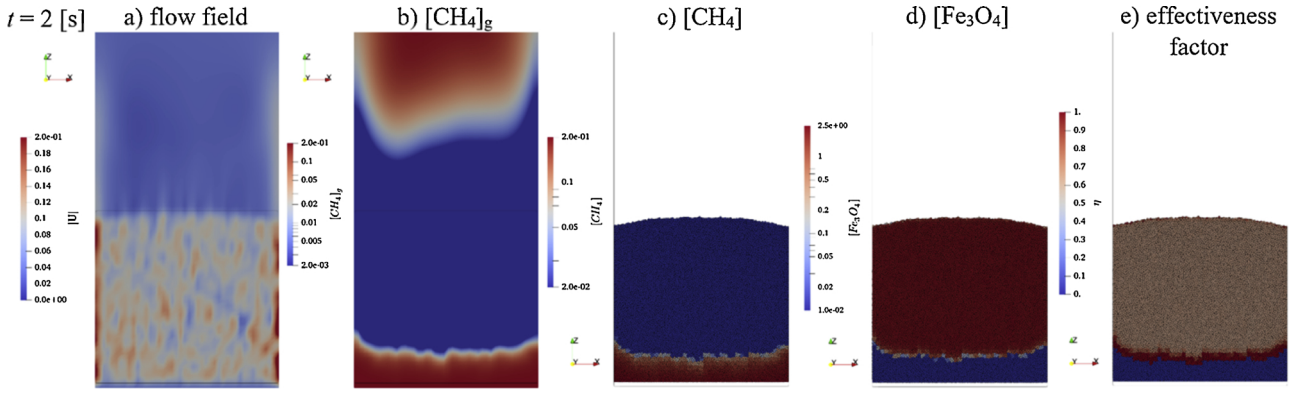

Fig. 14. Results considering a fixed bed reactor, a grain size of 10 nm, and a carrier particle size of 1 mm (a): magnitude of the velocity field, b): gas-phase CH4 concentration distribution, c): CH_4 concentration in the pores of the carrier particles, d): Fe_3O_4 concentration, e): effectiveness factor).

reaction rates considered (only for conversions higher than 0.8 does the simple model deviate more significantly from the simulation data such that lower and higher effectiveness factors for the 10 nm and 1 µm grains would be advisable, respectively). This can be explained by the overall fast reaction in all three scenarios, which leads to a significant CH_4 depletion in the pores of the particles.

4. Conclusions

We presented a multiscale modeling framework for fluidized bed reactors with specific application to the use of iron oxide (Fe_3O_4) nanoparticles as reactive oxygen carrier particles in Chemical Looping Reforming (CLR) systems. The ultimate goal was to improve on current computational materials design initiatives by not only focusing on fundamental materials properties, but also the use of materials in specific processes.

At the atomic scale, kinetic Monte Carlo simulations were run to provide kinetic data for macroscopic flow models. The kinetic Monte Carlo simulations were partly based on DFT calculations on CH_4 and H_2 reactions at Fe_3O_4. Due to challenges in achieving converged DFT results some simplifications were made. The resulting overall surface reaction rates were post-processed for use in macroscopic models with the goal to integrate process information with materials information. It was found that this can be done in a reasonably straightforward manner and that – although several approximations and simplifications were made in our test case presented here – this can be made increasingly more accurate by well-defined corrections to the simple zeroth-order model.

The key conclusions from our macroscopic modeling, i.e., the results of our intra-particle and multiphase flow simulations, can be summarized as follows: for typical fluidized bed CLR systems that rely on methane conversion over Fe_3O_4, intra-particle effectiveness factors may be safely set to unity. In case intra-particle transport effects are expected to be significant, a simple model for this effectiveness factor [49] is suitable and most computationally efficient. However, for the CLR systems investigated in our present work, meso-scale mixing effects should not be neglected. As we have shown, these effects reduce the reaction rate (estimated from a perfect mixing model) by more than 40%. Also, we have shown that for a typical CLR fixed bed reactor with 1 µm carrier particles, the intra-particle effectiveness factor varies locally, and approaches unity near the reaction front. This is due to the sensitivity of the effectiveness factor to the solids concentration, which is smallest near the reaction front. Clearly, a spatially varying effectiveness factor should be taken into account for such reactors. Our ongoing work related to reactive gas-particle flow models includes strategies to avoid tracking all particles in the flow field, e.g., by adopting parcel-based and systematic coarsening approaches [52]. In future studies, this may allow researchers and engineers to rely on predictions of PU-EL-based simulations of pilot-, or even full-scale reactors.

The approach of computationally testing materials both for their fundamental microscopic properties and their use in flow models of realistic reactor conditions, ultimately leads to better descriptors of materials performance that can be used in future materials screening activities. This is especially relevant for performance with respect to economic and ecological parameters, since they critically depend on the size of the reactor, as well as the conversion that can be achieved.

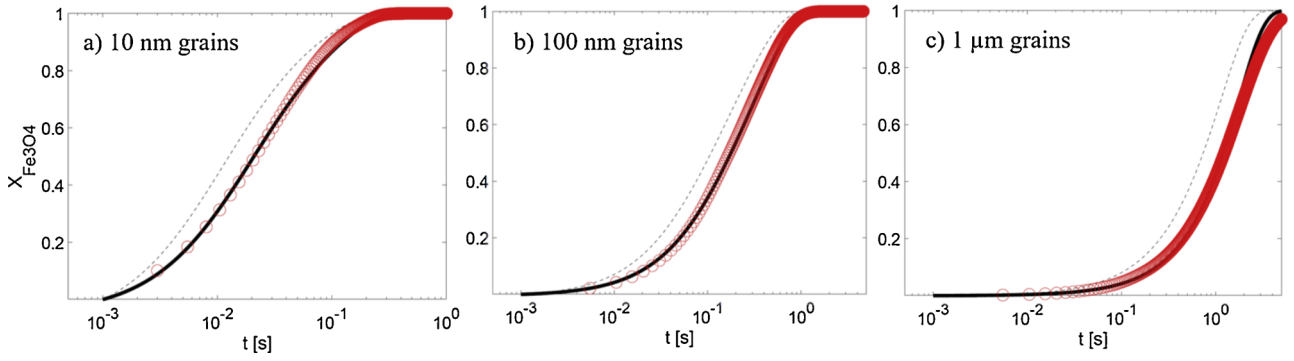

Fig. 15. Average Fe_3O_4 conversion in a fluidized bed versus time for different grain sizes (base case scenario; red dots: simulation output, dashed line: model assuming perfect mixing of gas and particle phase, solid line: model accounting for a meso-scale effectiveness factor with $\eta_{meso} = 0.58$). (For interpretation of the references to colour in this figure legend, the reader is referred to the web version of this article.)

Acknowledgements

We thank Paul Inge Dahl and Julian Tolchard for useful discussions on the synthesis and characterization of embedded nanoparticles. We acknowledge funding by a European Union FP7 grant: NanoSim – A Multiscale Simulation-Based Design Platform for Cost-Effective CO2 Capture Processes using Nano-Structured Materials (project number 604656). UNINETT Sigma2 – the National Infrastructure for High Performance Computing and Data Storage in Norway is acknowledged for generous grants of computer time (projects NN9353K and NN9355K).

References

[1] J. Adanez, A. Abad, F. Garcia-Labiano, P. Gayan, L.F. de Diego, Prog. Energy Combust. Sci. 38 (2012) 215–282.
[2] M. Rydén, A. Lyngfelt, T. Mattisson, Energy Fuels 22 (2008) 2585–2597.
[3] D. Wen, P. Song, K. Zhang, J. Qian, J. Chem. Technol. Biotechnol. 86 (2011) 375–380.
[4] M. Kirchhoff, U. Specht, G. Veser, M. Laudon, B. Romanowicz (Eds.), NSTI-Nanotech 2004, vol. 3, Technical Proceedings, 2004, pp. 268–271 http://www.nsti.org/publications/Nanotech/2004/pdf/B3-72.pdf.
[5] M. Kirchhoff, U. Specht, G. Veser, Nanotechnology 16 (2005) S401–S408.
[6] G. Veser, Catal. Today 157 (2010) 24–32.
[7] R.D. Solunke, G. Veser, Energy Fuels 23 (2009) 4787–4796.
[8] S. Bhavsar, M. Najera, G. Veser, Chem. Eng. Technol. 35 (2012) 1281–1290.
[9] A.J. Zarur, J.Y. Ying, Nature 403 (2000) 65–67.
[10] A.J. Zarur, H.H. Hwu, J.Y. Ying, Langmuir 16 (2000) 3042–3049.
[11] L. Huang, M. Tang, M. Fan, H. Cheng, Appl. Eng. 159 (2015) 132–144.
[12] J.-J. Tang, B. Liu, J. Phys. Chem. C 120 (2016) 6642–6650.
[13] Z. Cheng, L. Qin, M. Guo, M. Xu, J.A. Fan, L.-S. Fan, Phys. Chem. Chem. Phys. 18 (2016) 32418–32428.
[14] A. Rydén, A. Lyngfelt, T. Mattisson, D. Chen, A. Holmen, D. Bjørgum, Int. J. Greenh. Gas Control. 2 (2017) 21–36.
[15] S. Curtarolo, G.L.W. Hart, M.B. Nardelli, N. Mingo, S. Sanvito, O. Levy, Nature Mater. 12 (2013) 191–201.
[16] L.C. Lin, A.H. Berger, R.L. Martin, J. Kim, J.A. Swisher, K. Jariwala, C.H. Rycroft, A.S. Bhown, M.W. Deem, M. Haranczyk, B. Smit, Nature Mater. 11 (2012) 633–641.
[17] P. Kočí, M. Isoz, M. Plachá, A. Arvajová, M. Václavík, M. Svoboda, E. Price, V. Novák, D. Thompsett, Catal. Today 320 (2019) 165–174.
[18] S. Das, N.G. Deen, J.A.M. Kuipers, Catal. Today 273 (2016) 140–150.
[19] J.F. Joly, F. Giroudière, F. Bertoncini, Catal. Today 218–219 (2013) 153–161.
[20] I. Rossetti, Catal. Today 308 (2018) 20–31.
[21] EMMC – The European Materials Modelling Council, https://emmc.info.
[22] Roadmap Chemical Reaction Engineering, Dechema, (2017) https://dechema.de/dechema_media/Downloads/Positionspapiere/Reaktionstechnik_Roadmap_2017_en.pdf.
[23] A.G. Dixon, Chem. Eng. Sci. 168 (2017) 156–177.
[24] T. Maffei, G. Gentile, S. Rebughini, M. Bracconi, F. Manelli, S. Lipp, A. Cuoci, M. Maestri, Chem. Eng. J. 283 (2016) 1392–1404.
[25] M. Hettel, E. Daymo, O. Deutschmann, Comp. Chem. Eng. 109 (2018) 166–178.
[26] S. Sundaresan, Annu. Rev. Fluid Mech. 35 (2003) 63–88.
[27] W. Holloway, S. Sundaresan, Chem. Eng. Sci. 82 (2012) 132–143.
[28] S. Cloete, S.T. Johansen, S. Amini, Powder Technol. 269 (2015) 153–165.
[29] G. Kresse, J. Hafner, Phys. Rev. B 47 (1993) 558–561.
[30] G. Kresse, J. Hafner, Phys. Rev. B 49 (1994) 14251–14269.
[31] G. Kresse, J. Furthmüller, Comput. Mater. Sci. 6 (1996) 15–50.
[32] G. Kresse, J. Furthmüller, Phys. Rev. B 54 (1996) 11169–11186.
[33] P.E. Blöchl, Phys. Rev. B 50 (1994) 17953–17979.
[34] G. Kresse, D. Joubert, Phys. Rev. B 59 (1999) 1758–1775.
[35] S.L. Dudarev, G.A. Botton, S.Y. Savrasov, C.J. Humphreys, A.P. Sutton, Phys. Rev. B 57 (1998) 1505–1509.
[36] S.M.O. Souvi, M. Badawi, J.-F. Paul, S. Cristol, L. Cantrel, Surf. Sci. 610 (2013) 7–15.
[37] A. Kiejna, T. Pabisiak, J. Phys. Condens. Matter 24 (2012) 095003.
[38] G. Rollmann, A. Rohrbach, P. Entel, J. Hafner, Phys. Rev. B 69 (2004) 165107.
[39] M.-T. Nguyen, N. Seriani, S. Piccinin, R. Gebauer, J. Chem. Phys. 140 (2014) 064703.
[40] L. Ling, J. Song, S. Zhao, R. Zhang, B. Wang, RSC Adv. 4 (2014) 22411–22418.
[41] G. Henkelman, H. Jónsson, J. Chem. Phys. 113 (2000) 9901–9904.
[42] X. Yu, C.-F. Huo, Y.-W. Li, J. Wang, H. Jiao, Surf. Sci. 606 (2012) 872–879.
[43] J. Noh, O.I. Osman, S.G. Aziz, P. Winget, J.-L. Brédas, Chem. Mater. 27 (2015) 5856–5867.
[44] A.P.J. Jansen, An Introduction to Kinetic Monte Carlo Simulations of Surface Reactions, Springer, 2012.
[45] K. Reuter, M. Scheffler, Phys. Rev. B 73 (2006) 045433.
[46] M.J. Hoffmann, S. Matera, K. Reuter, Computer Phys. Commun. 185 (2014) 2138–2150.
[47] M.K. Sabbe, M.-F. Reyniers, K. Reuter, Catal. Sci. Technol. 2 (2012) 2010–2024.
[48] M. Andersen, C. Panosetti, K. Reuter, Front. Chem. 7 (2019) 202.
[49] W. Yang, S. Cloete, J. Morud, S. Amini, Int. J. Chem. React. Eng. 14 (2016) 331–342.
[50] T. Forgber, B. Mohan, C. Kloss, S. Radl, Granul. Matter 19 (2017) 14.
[51] S. Radl, F. Municchi, S. Cloete, H. Cloete, S. Andersson, J.F. Morgado, T. Gurker, R. Quinta-Ferreira, C. Kloss, C. Goniva, S. Amini, Comput. Aided Chem. Eng. 43 (2018) 247–252.
[52] A. Ozel, J. Kolehmainen, S. Radl, S. Sundaresan, Chem. Eng. Sci. 155 (2016) 258–267.